High-resolution Scanning Transmission EBIC Analysis of Misfit Dislocations at Perovskite pn-Heterojunctions

T Meyer[1], B Kressdorf[2], J Lindner[2], P Peretzki[1], V Roddatis[2], C Jooss[2] and M Seibt[1]

[1] 4th Institute of Physics – Solids and Nanostructures, University of Goettingen, Friedrich-Hund-Platz 1, 37077 Goettingen, Germany
[2] Institute of Materials Physics, University of Goettingen, Friedrich-Hund-Platz 1, 37077 Goettingen, Germany

tmeyer@uni-goettingen.de

Abstract. Fundamental losses of photovoltaic energy conversion are transmission of sub band gap photons and thermalisation which are the underlying physics of the Shockley-Queisser limit defining maximum conversion efficiency of single-junction solar cells. Strongly correlated materials such as perovskites are promising candidates to exceed this limit by exploiting (i) long wavelength light absorption and (ii) the existence of long-living intraband excitations indicating that harvesting hot excess carriers might be feasible in such systems. In this work, we study pn-heterojunctions produced from $Pr_{1-x}Ca_xMnO_3$ on $SrTi_{1-y}Nb_yO_3$ by means of microscopic techniques. Such systems exhibit relevant quantities such as space charge layer width, screening lengths and excess carrier diffusion lengths in the 1-10 nm range which makes the use of standard methods such as electron beam induced current a challenging task. We report scanning transmission electron beam induced current experiments of misfit dislocations at the heterojunction. The dislocation-induced reduction of the charge collection is studied with nanometer spatial resolution. Effects of surface recombination and the heterojunction electric field are discussed.

1. Introduction

Transition metal oxide perovskites, in particular manganites, became popular in the 1950s due to their extraordinary magnetic properties [1]. Ever since then the interest in this class of strongly correlated materials has grown continuously and various extraordinary phenomena such as high-temperature superconductivity [2], colossal magnetoresistance [3], and photovoltaic activity [4] have been discovered. One reason for the diversity of research projects related to perovskites is the high adjustability of different degrees of freedom: The ideal perovskite structure ABC_3 is cubic with A occupying the primitive, B the body-centred, and C, symbolising oxygen for all compounds considered in this work, the face-centred sites. In addition, tetragonal and even orthorhombic perovskites exist resulting from small lattice deformations. The latter are typically related to rotations and distortions of the octahedron spanned by species C and depend highly on the particular choice of constituents as well as doping of the respective lattice sites [5]. Thus, bonding lengths and angles of neighbouring atoms can be adjusted by the samples' stoichiometry resulting in different overlaps of orbitals and hence a tunable interplay of exchange interactions [6-8].

Using organic halide compounds, the efficiency of perovskite based solar cells has been increased beyond 20% during the last decade [9] offering a competitive solution to silicon solar cells. Still,

achieving long-term stability and explaining the underlying physical transport processes remain open challenges. Despite much lower photovoltaic energy conversion efficiencies, transition metal oxide perovskites can be considered as a model system to accomplish the second task. In fact, it has been shown that $Pr_{1-x}Ca_xMnO_3$ exhibit strong infrared absorption [10]. While a thorough review on manganites in general can be found in [11], this article focuses on the particular compound $Pr_{0.66}Ca_{0.34}MnO_3$, subsequently referred to as PCMO, exhibiting a positive Seebeck coefficient and thus being considered as a p-type material [12]. Used as an absorbing material, PCMO shows a tremendously better photovoltaic performance in a charge-ordered state where the lattice distortions mentioned above become cooperative [13,14]. Most noticeably, the corresponding polaronic excitations are intraband transitions. Although they could potentially relax via phonon scattering, they seem to be stabilised by the cooperative configuration. Hence, the basic assumption of hot carrier thermalisation being faster than typical charge collection times resulting in the Shockley-Queisser limit [15] might be overcome in strongly correlated materials. Consequently, perovskites are a promising candidate to exceed this limitation. In this work, the considered PCMO films are grown on $SrTi_{0.998}Nb_{0.002}O_3$ substrates, subsequently referred to as STNO, an n-type material showing polaronic transport behaviour [16]. Besides the advantageous characteristics for photovoltaic applications mentioned above, due to typically high doping levels and the low mobility of polaronic charge carriers, important physical properties of the resulting PCMO-STNO heterojunction such as the space charge region width as well as the screening and excess carrier diffusion lengths are in the 1-10 nm range [17] demanding for high-resolution technique to investigate the fundamental electric transport phenomena.

Electron beam induced current (EBIC) is a widespread technique to map the electronic response of rectifying devices stimulated by a local excitation with energetic electrons and can be easily implemented in scanning electron microscopes (SEM) [18]. Despite the well-focussed incident beam, resolutions in the nanometer range cannot be achieved, which is due to multiple scattering of electrons in the material resulting in a pear-shaped spread of the energy deposited by the beam [19]. The generation volume increases with increasing acceleration voltage, also referred to as the Bethe limit [20]. Complementary approaches to decrease the latter have been made to decrease the samples' dimension along the beam propagation direction resulting in transmission of the impinging electrons before the beam spreads severely [21,22]. This idea is not only applicable to EBIC but also to cathodoluminescence (CL) measurements [23] and in contrast to non-transmitting methods the generation volume decreases with increasing acceleration voltage, also referred to as the Goldstein limit [24].

In this work, we present how scanning transmission EBIC (STEBIC) can be applied to PCMO-STNO heterojunctions in order to visualise enhanced recombination at misfit dislocations on the nanometer scale.

2. Experiment

A 100 nm thick $Pr_{0.66}Ca_{0.34}MnO_3$ film has been deposited on a commercial $SrTi_{0.998}Nb_{0.002}O_3$ substrate by reactive Xe-ion beam sputtering with an oxygen partial pressure of $1.4 \cdot 10^{-4}$ mbar at 700° C. Subsequently, the heterojunction has been annealed for 20 hours at 900° C in air and equipped with a 200 nm thick Pt front contact layer via room temperature Xe-ion beam sputtering.

TEM lamellae have been prepared on DENSsolutions four contacts biasing chips suitable for the Lightning D7+ holder inside an FEI Nova 600 NanoLab Dual Beam FIB and investigated with a Philips CM200 UT (BF-TEM) and an FEI Titan80-300 (DF-STEM and EBIC) at 200 kV and 80 kV/300 kV, respectively. Figure 1 shows a DF-STEM image of a final TEM lamella after Ga-ion milling following the recipe summarised in table 1 and reactive plasma cleaning for 2 min. Electron energy loss spectroscopy confirms a quite uniform lamella thickness of roughly 40 nm.

In order to measure the EBIC signal, the DENSsolutions holder was connected to a Stanford Research Systems SR570 current preamplifier, which converts the input current into an output voltage.

The latter was read out using a Keithley 2000 digital multimeter controlled by a homemade National Instruments LabVIEW script. Synchronously, the electron beam position inside the TEM was adjusted by a homemade Gatan DigitalMicrograph script communicating with the LabVIEW script via a shared folder.
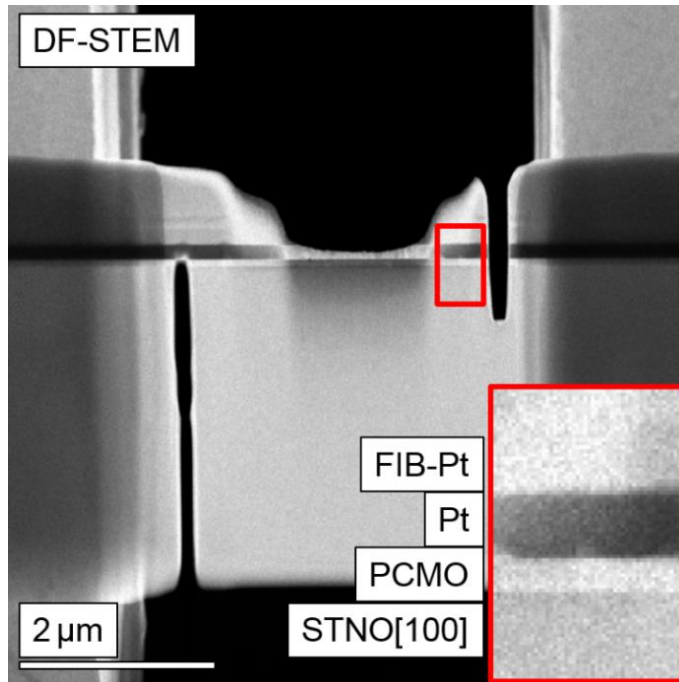

Figure 1. DF-STEM image of the FIB-prepared lamella: The enlargement of the small rectangular box marked illustrates the different layers of the sample. Vertical cuts have been made utilising low-dose (30 pA) Ga-ion milling with an acceleration voltage of 30 kV in order to prevent short circuits across the pn-junction.

Acceleration Voltage (kV)	Ga-ion beam current (pA)	Tilt offset (°)	Residual thickness (nm)
30	300	1.2	800
30	100	1.2	300
5	29	2	<50

Table 1. Milling recipe for the TEM lamellae preparation using Ga-ions. The residual thickness values are rough estimations obtained by the measurement tool of the FIB software and should be considered as a guide.
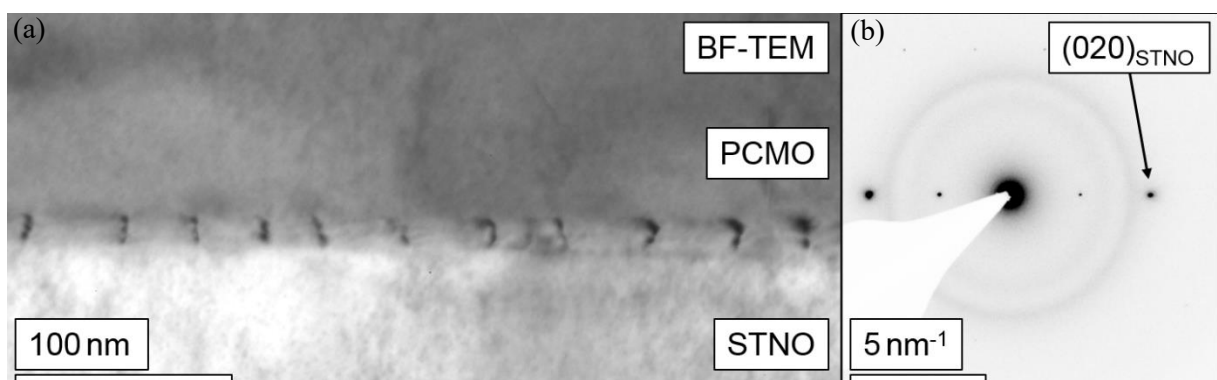

Figure 2. (a) BF-TEM image of the pn-junction revealing frequently occurring misfit dislocations with (b) corresponding diffraction pattern. Only the systematic row of $(010)_{STNO}$ reflections is excited, i.e. the interface is inclined by 20° with respect to the incident electron beam leading to the vertical elongation of the dark contrasts.

3. Results and Discussion

Given the high spatial resolution of STEBIC, local variations of the junction's short-circuit current can be detected. Typical causes for such variations are perturbations of the crystal symmetry resulting in enhanced recombination of excess charge carriers [25]. Due to the lattice misfit between film and substrate of approximately f = -1.5% [26], defect formation to relax the corresponding stress are likely to occur. In fact, in PCMO/STNO thin film couples various relaxation possibilities like oxygen vacancy formation [27], twinning [28], and plastic relaxation due to dislocations [12] have been reported. Figure 2 shows that misfit dislocations occur frequently under the growth conditions described in the previous section. The mean distance between the observed dislocations of 33 nm is only 27% larger than the characteristic dislocation distance d = a/f = 26 nm for total stress relaxation via misfit dislocation formation (with a being the mean in-plane lattice constant of PCMO [29]). Hence, a substantial fraction of the epitaxial stress is relaxed via this channel.

High-resolution DF-STEM images reveal that, despite having the same Burgers vector $[010]_{STNO}$, the dislocations have different characters: Figure 3(b) shows an interfacial dislocation (subsequently referred to as 'dislocation I') with an added half plane in the film. Since the unit cell of PCMO is larger than in STNO due to alternatingly tilted oxygen octahedra [30], the Burgers vector $[010]_{STNO}$ corresponds to a partial dislocation in the PCMO which is probably accompanied by a stacking fault in the tilt system. The related strain could induce chemical disorder, e.g. vacancies, leading to the dark vertical contrast emerging at the interface. On the contrary, the core of the buried dislocation in figure 4(b) (subsequently referred to as 'dislocation II') lies approximately five unit cells below the junction and the alternating tilting pattern of the PCMO film above seems to be undisturbed. The corresponding EBIC maps in figure 3(a) and figure 4(a) show that the induced recombination behaviour is significantly different.

Dislocation I leads to a small kink in the EBIC signal marked by the black circle but no medium range effect. A straight forward explanation would be to assume that dislocation I does not introduce deep states into the gap of PCMO. It should be kept in mind, however, that the screening length in PCMO [31] as well as the excess carrier diffusion length [14] are in the nanometer range indicating that the effect of deep states on the EBIC signal should be small. In contrast, dislocation II reduces the EBIC signal by roughly 30% in the vicinity of the core as shown by the averaged horizontal line
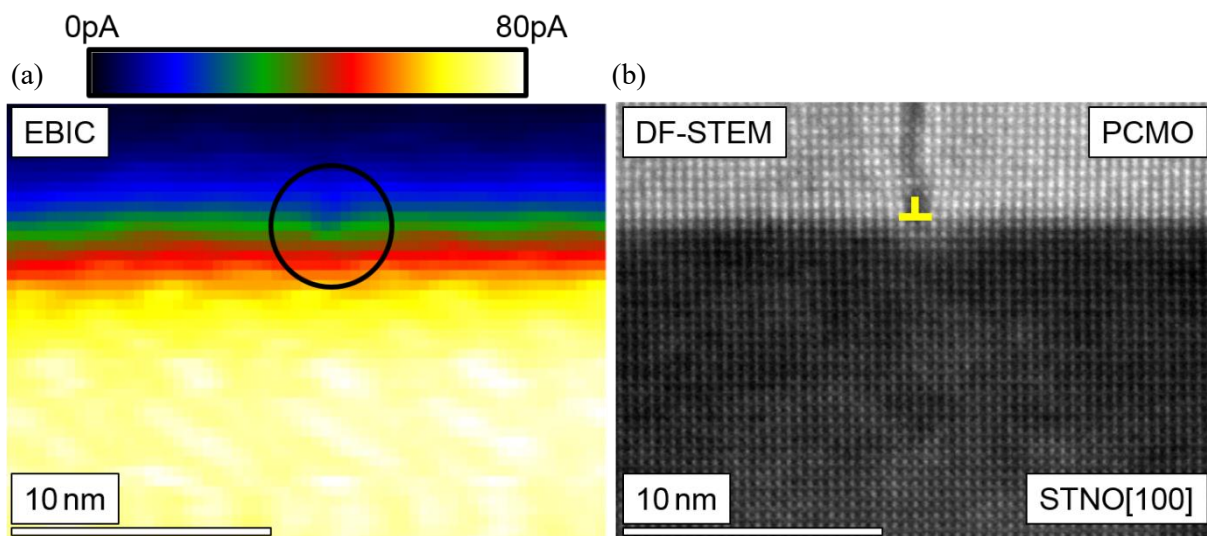

Figure 3. (a) EBIC map of an interfacial edge dislocation and (b) the corresponding DF-STEM micrograph. The dislocation is accompanied by a stacking fault in the PCMO layer due to its larger unit cell and has little effect on the EBIC signal.
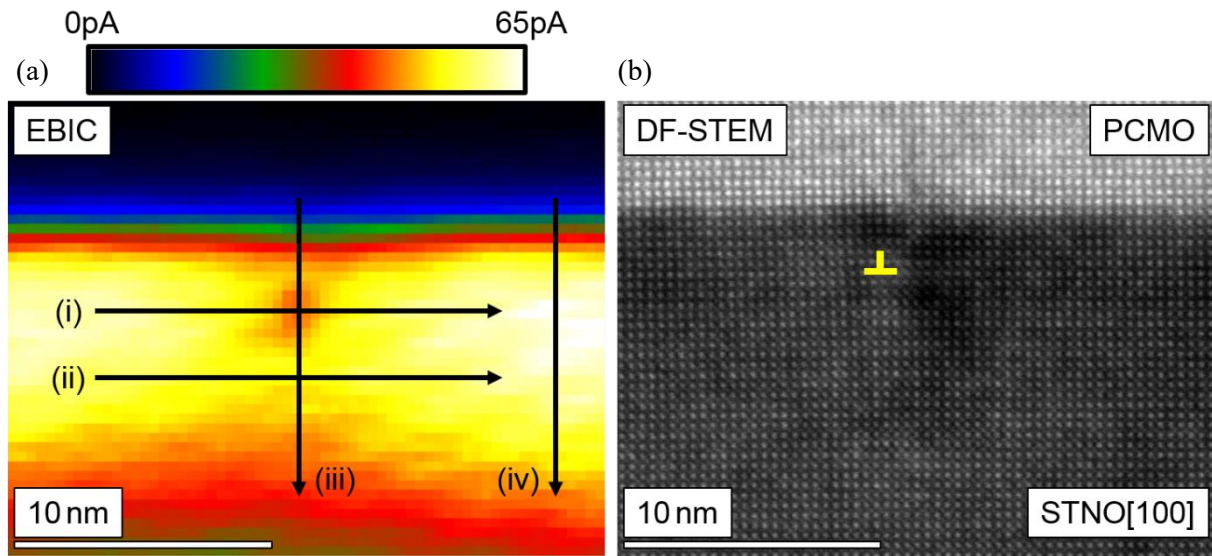
Figure 4. (a) EBIC map of a buried edge dislocation and (b) the corresponding DF-STEM micrograph. The dislocation reduces the EBIC signal significantly. The black arrows in (a) indicate spatial directions considered in figure 5.
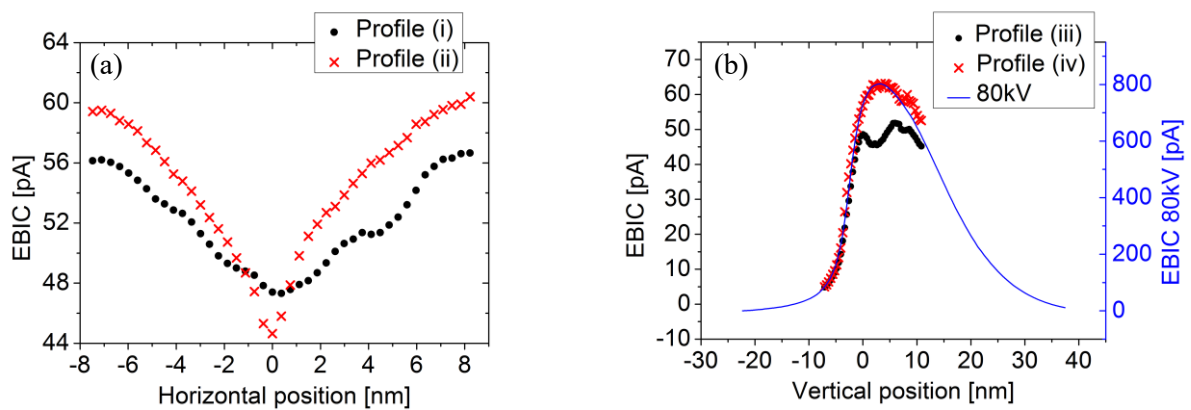

Figure 5. EBIC profile taken along (a) the horizontally aligned arrows in figure 4(a) (averaged over five lines) and (b) along the vertically aligned arrows in figure 4(a) (averaged over five lines); roman numbers refer to arrows in figure 4(a). In addition, the cyan curve in (b) shows an EBIC profile taken across the pn-heterojunction of a different lamella with 80 kV instead of 300 kV in a region without any dislocations. Note that the EBIC magnitude for 80 kV is higher due to a different beam current and inelastic scattering cross section.

profile (i) in figure 5(a). The apparently stronger recombination behaviour of dislocation II can be partially explained by the slightly higher excess carrier diffusion length of STNO [14]. However, the intersection of the profiles in figure 5(a) shows that the dislocation induced recombination below the core is stronger than at its actual position, which is not the case for dislocation I. A possible explanation for this behaviour is the interplay between the dislocation itself and the electric field of the space charge region of the pn-heterojunction. The latter is supposed to be maximal at the chemical interface and to decay monotonously resulting in a potentially smaller charge carrier separation and hence an effectively larger influence of the dislocation induced recombination. The black and yellow vertical profiles in figure 5(b) confirm indeed that the main part of the reduced EBIC signal is located inside the space charge region expected to extend at least 10 nm into the STNO [14].

Finally, we would like to emphasise the reproducibility of the experiment and an experimental evidence that beam spread effects of the electron probe resulting from (multiple) scattering can be ruled out as the resolution-limiting effect in these experiments: The cyan curve in figure 5(b) shows the EBIC profile across the pn-heterojunction taken from another lamella with an acceleration voltage of 80 kV instead of 300 kV. Since any beam broadening effects are expected to strongly depend on the acceleration voltage, the strong matching of the shape of the two measured profiles provides evidence that beam spread is negligible as well as that different lamellae lead to identical results within experimental error.

4. Summary and Conclusion

We have reported an experimental setup achieving a resolution of at least a few nanometers by means of scanning transmission EBIC (STEBIC) investigations offering the possibility to map the recombination and transport behaviour of transition metal oxide perovskites with relevant physical quantities in the 1-10 nm range. The spatial extension of STEBIC signals is limited by sample properties such as the excess carrier diffusion lengths of the materials rather than by the size of the generation volume resulting from electron scattering. This is evidenced by showing that the shape of the resulting STEBIC profiles is independent of the chosen acceleration voltage.

Applying this technique to misfit dislocations, we have shown that the position of the dislocation core can have a tremendous impact on the resulting excess carrier recombination. In fact, in contrast to interfacial dislocations, buried dislocations shifted inside the STNO show an enhanced EBIC decrease and, in addition, a medium range recombination effect. The obvious effect of different bulk recombination properties of the two materials on the dislocation recombination behaviour has been discussed qualitatively. Nevertheless, the underlying mechanisms are not yet fully understood.

A sufficiently precise model has to describe the concerted action of (i) the presence of the pn-junction's space charge region, (ii) potential surface recombination at the two lamella surfaces, (iii) additional electric field below the lamella surfaces as a result of Fermi level pinning, and (iv) the formation of 'dead layers' due to sample preparation. The latter have been discussed to some extent in [19] and related to experimental results obtained on the PCMO/STNO system and a silicon pn-junction. Surface recombination in the absence of any electric field can be described in terms of a Green's function approach which has been evaluated numerically in [32] by placing a large number of mirror charges in order to satisfy the boundary conditions at the surfaces resulting in a quantitative description of EBIC signals obtained outside the charge collecting junction's space charge region. Other models considering effective excess carrier diffusion lengths or a surface recombination factor in the EBIC profile have been introduced in [33] and [34]. Furthermore, sophisticated and quantitatively proven models of excess carrier recombination at dislocations [35] assume excitations in the neutral bulk and cannot be readily adopted to the situation in our experiments. Hence, all existing models are based on the assumption of exciting the sample outside the electric field of the space charge region. A possibility to fill this gap is the employment of finite element simulations, which we are currently working on.

References

[1]   van Santen J H and Jonker G H 1950 *Physica* **16** 337
[2]   Bednorz J G and Müller K A 1986 *Z. Physik B - Condensed Matter* **64** 189
[3]   von Helmolt R, Wecker J, Holzapfel B, Schultz L and Samwer K 1993 *Phys. Rev. Lett.* **71** 2331
[4]   Sawa A, Fujii T, Kawasaki M and Tokura Y 2005 *Appl. Phys. Lett.* **86** 112508
[5]   Röder H, Zang J and Bishop A R 1996 *Phys. Rev. Lett.* **76** 1356
[6]   Zener C 1951 *Phys. Rev.* **82** 403

[7]   Anderson P W and Hasegawa H 1955 *Phys. Rev.* **100** 675

[8]   Gennes P G 1960 *Phys. Rev.* **118** 141

[9]   Abdi-Jalebi M *et al.* 2018 *Nature* **555** 497

[10]   Mildner S, Hoffmann J, Blöchl P, Techert S and Jooss C 2015 *Phys. Rev. B* **92** 035145

[11]   Dagotto E 2013 *Nanoscale Phase Separation and Colossal Magnetoresistance* (Berlin: Springer Science & Business Media)

[12]   Yamada S, Arima T H, Ikeda H and Takita K 2000 *Journal of the Physical Society of Japan* **69** 1278-1281

[13]   Raiser D, Mildner S, Ifland B, Sotoudeh M, Blöchl P, Techert S and Jooss C 2017 *Adv. Energy Mater.* **7** 1602174

[14]   Ifland B, Hoffmann J, Kressdorf B, Roddatis V, Seibt M and Jooss C 2017 *New J. Phys.* **19** 063046

[15]   Shockley W and Queisser H J 1961 *Journal of Applied Physics* **32** 510

[16]   Bi C Z, Ma J Y, Yan J, Fang X, Zhao B R, Yao D Z and Qiu X G 2006 *Journal of Physics: Condensed Matter* **18** 2553

[17]   Ifland B, Peretzki P, Kressdorf B, Saring P, Kelling A, Seibt M and Jooss C 2015 *Beilstein Journal of Nanotechnology* **6** 1467

[18]   Leamy H J 1982 *Journal of Applied Physics* **53** R51

[19]   Donolato C 1981 *phys. stat. sol. (a)* **65** 649

[20]   Bethe H 1930 *Annalen der Physik* **4** 325

[21]   Cabanel C, Brouri D and Laval J 2006 *The European Physical Journal* **34** 107

[22]   Peretzki P, Ifland B, Jooss C and Seibt M 2017 *Phys. Status Solidi RRL* **11** 1600358

[23]   Chin A K, Temkin H and Roedel R J 1979 *Appl. Phys. Lett.* **34** 476

[24]   Goldstein J I 1977 *Scanning Electron Microscopy* **1977** 315

[25]   Falkenberg M A, Schuhmann H, Seibt M and Radisch V 2010 *Review of Scientific Instruments* **81** 063705

[26]   Ifland B, Hoffmann J, Kramer T, Scherff M, Mildner S and Jooss C 2015 *J. Nanomaterials* **3** 1

[27]   Chandrasena R U *et al.* 2017 *Nano Lett.* **17** 794

[28]   Hoffmann J, Moschkau P, Mildner S, Norpoth J, Jooss C, Wu L and Zhu Y 2014 *Mater. Res. Express* **1** 046403

[29]   Jirak Z, Krupicka S, Simsa Z, Glouha M and Vratislav S 1985 *Journal of Magnetism and Magnetic Materials* **53** 153

[30]   Glazer A M 1972 *Acta Crystallographica Section B* **28** 3384

[31]   Saucke G, Norpoth J, Jooss C, Su D and Zhu Y 2012 *Phys. Rev. B* **85** 165315

[32]   Tan C C, Ong V K and Radhakrishnan K 2013 *Prog. Photovolt: Res. Appl.* **21** 986

[33]   Donolato C 1983 *Appl. Phys. Lett.* **43** 120

[34]   Ong V K S, Phang J C H and Chan D S H 1994 *Solid-State Electronics* **37** 1

[35]   Kveder V V, Kittler M and Schröter W 2001 *Phys. Rev. B*. **63** 115208